



HAL
open science

A fusion of the *Bacteroides fragilis* ferrous iron import proteins reveals a role for FeoA in stabilizing GTP-bound FeoB

Alex Sestok, Janae Brown, Juliet Obi, Sean O'sullivan, Elsa Garcin, Daniel Deredge, Aaron Smith

► To cite this version:

Alex Sestok, Janae Brown, Juliet Obi, Sean O'sullivan, Elsa Garcin, et al.. A fusion of the *Bacteroides fragilis* ferrous iron import proteins reveals a role for FeoA in stabilizing GTP-bound FeoB. *Journal of Biological Chemistry*, 2022, 298 (4), pp.101808. 10.1016/j.jbc.2022.101808 . hal-03733773

HAL Id: hal-03733773

<https://amu.hal.science/hal-03733773>

Submitted on 21 Jul 2022

HAL is a multi-disciplinary open access archive for the deposit and dissemination of scientific research documents, whether they are published or not. The documents may come from teaching and research institutions in France or abroad, or from public or private research centers.

L'archive ouverte pluridisciplinaire **HAL**, est destinée au dépôt et à la diffusion de documents scientifiques de niveau recherche, publiés ou non, émanant des établissements d'enseignement et de recherche français ou étrangers, des laboratoires publics ou privés.



Distributed under a Creative Commons Attribution 4.0 International License



A fusion of the *Bacteroides fragilis* ferrous iron import proteins reveals a role for FeoA in stabilizing GTP-bound FeoB

Received for publication, October 1, 2021, and in revised form, March 3, 2022. Published, Papers in Press, March 8, 2022.

<https://doi.org/10.1016/j.jbc.2022.101808>

Alex E. Sestok^{1,‡}, Janae B. Brown^{1,‡}, Juliet O. Obi² , Sean M. O'Sullivan¹, Elsa D. Garcin^{1,3} , Daniel J. Deredje², and Aaron T. Smith^{1,*} 

From the ¹Department of Chemistry and Biochemistry, University of Maryland, Baltimore County, Baltimore, Maryland, USA; ²Department of Pharmaceutical Sciences, University of Maryland School of Pharmacy, Baltimore, Maryland, USA; ³Laboratoire d'Information Génomique et Structurale, UMR7256, Aix-Marseille Université, Campus de Luminy, Marseille, France

Edited by Ruma Banerjee

Iron is an essential element for nearly all organisms, and under anoxic and/or reducing conditions, Fe²⁺ is the dominant form of iron available to bacteria. The ferrous iron transport (Feo) system is the primary prokaryotic Fe²⁺ import machinery, and two constituent proteins (FeoA and FeoB) are conserved across most bacterial species. However, how FeoA and FeoB function relative to one another remains enigmatic. In this work, we explored the distribution of *feoAB* operons encoding a fusion of FeoA tethered to the N-terminal, G-protein domain of FeoB *via* a connecting linker region. We hypothesized that this fusion poises FeoA to interact with FeoB to affect function. To test this hypothesis, we characterized the soluble NFeoAB fusion protein from *Bacteroides fragilis*, a commensal organism implicated in drug-resistant infections. Using X-ray crystallography, we determined the 1.50-Å resolution structure of B_fFeoA, which adopts an SH3-like fold implicated in protein-protein interactions. Using a combination of structural modeling, small-angle X-ray scattering, and hydrogen-deuterium exchange mass spectrometry, we show that FeoA and NFeoB interact in a nucleotide-dependent manner, and we mapped the protein-protein interaction interface. Finally, using guanosine triphosphate (GTP) hydrolysis assays, we demonstrate that B_fNFeoAB exhibits one of the slowest known rates of Feo-mediated GTP hydrolysis that is not potassium-stimulated. Importantly, truncation of FeoA from this fusion demonstrates that FeoA-NFeoB interactions function to stabilize the GTP-bound form of FeoB. Taken together, our work reveals a role for FeoA function in the fused FeoAB system and suggests a function for FeoA among prokaryotes.

Nearly all living organisms rely on iron acquisition and utilization for vital cellular processes from aerobic cellular respiration, N₂ fixation, gene regulation, and DNA biosynthesis (1–3). Given the versatile functionality of iron, this element may be used as an ionic cofactor and bound by biological macromolecules such as in ribonucleotide reductases

(4), utilized in [Fe-S] clusters such as those in nitrogenase (5) or the electron transport chain (6), and even chelated in protoporphyrin-IX (heme) and bound to O₂-carrying proteins such as hemoglobin and myoglobin (7). However, a prerequisite of iron incorporation into proteins is the acquisition of this element, which can be challenging. While ferric iron (Fe³⁺) is predominantly present in oxic environments, it is highly insoluble (K_{sp} ca. 10⁻¹⁸ M at pH 7.0) (1, 8). Conversely ferrous iron (Fe²⁺) is much more soluble (K_{sp} up to 0.1 M at pH 7.0) but is readily susceptible to oxidation and may be incredibly toxic to the cell *via* Fenton-like chemistry, if unregulated (1, 8, 9). As a result, organisms must exert both high energy and tight control over the iron acquisition process.

Historically, much work has been done to elucidate bacterial mechanisms of ferric iron and heme transport due to the link of these iron acquisition processes to pathogenesis. For example, it is well established that bacteria secrete small molecules called siderophores into the extracellular space to acquire ferric iron. These molecules have a high affinity for Fe³⁺ (K_{aff} ≥ 10³⁰ M⁻¹) and allow bacteria to compete against host Fe³⁺-binding proteins for ferric iron (8, 10, 11). Once acquired and delivered into the cytoplasm, Fe³⁺ can be released by degrading the siderophore or through reducing Fe³⁺ to Fe²⁺, which is accomplished by ferric iron reductases (8, 10–12). It is also well known that bacteria use dedicated transport systems to acquire heme. Heme acquisition is achieved through the use of hemophores, proteins that bind heme specifically and allow bacteria to compete for heme with host heme-binding proteins (13–15). Once delivered into the cytoplasm *via* a number of membrane-imbedded transporters, heme oxygenases then degrade heme to release iron for incorporation into proteins and metabolic enzymes (13–15).

In addition to Fe³⁺ and heme, bacteria can also transport and utilize Fe²⁺, although this process is far less well understood. The most widespread, dedicated prokaryotic machinery for Fe²⁺ import is the ferrous iron transport (Feo) system. The Feo system was first identified in 1987, and while *Escherichia coli* has a “canonical” arrangement of three genes (*feoA/B/C*), an arrangement in which only the *feoA* and *feoB* genes are present is far more common in bacteria (16–18). The function

[‡] These authors contributed equally to this work.

* For correspondence: Aaron T. Smith, smitha@umbc.edu.

Characterization of *B. fragilis* NFeoAB

of FeoA is unknown, but we do know that FeoA is an \approx 8-kDa, cytoplasmic β -barrel protein comprising an Src homology 3 (SH3)-like fold, which is commonly involved in protein-protein interactions. Given its structure, FeoA has been hypothesized to interact with FeoB to affect function (2, 3, 19, 20). FeoB is an \approx 85-kDa transmembrane (TM) protein consisting of a G-protein domain, a guanine dissociation inhibitor (GDI) domain, and a TM domain. The G-protein domain is responsible for binding and hydrolyzing guanosine triphosphate (GTP) (21), though recent studies have shown that some FeoB proteins are also capable of hydrolyzing ATP (22, 23). The GDI domain links the G-protein domain to the TM region and has been shown to increase the binding affinity of guanosine diphosphate (GDP) (24). Together, the G-protein domain and the GDI domain comprise what is termed NFeoB. Though the mechanism through which Fe^{2+} transport *via* FeoB occurs is unknown, *in vivo* studies indicate that nucleotide hydrolysis within the G-protein domain of NFeoB is important for Fe^{2+} transport. For example, a D123N variant in the G4 motif of *Ec*NFeoB was unable to rescue Fe^{2+} transport in a Δ *feoB* strain (21), while a variant in the G2 motif, T37A, also resulted in decreased GTPase activity and was unable to restore *in vivo* Fe^{2+} uptake (24). The TM region has not been structurally characterized but is likely the domain through which Fe^{2+} is translocated (25–27).

Despite our lack of mechanistic information, several studies have demonstrated the importance of the Feo system for the intracellular colonization, survival, and virulence of many pathogens. These infectious bacteria include, but are not limited to, *Legionella pneumophila* (28), *Campylobacter jejuni* (29), *Francisella tularensis* (30), avian pathogenic *E. coli* (31), *Shigella flexneri* (32), and *Streptococcus suis* (33). Interestingly, in some pathogens such as *Porphyromonas gingivalis* (the causative agent of gingivitis) (34) and *Bacteroides fragilis* (a commensal organism implicated in drug-resistant peritoneal infections) (35, 36), the *feo* operon is predicted to encode a single FeoAB fusion protein in which FeoA is naturally tethered to the soluble G-protein domain of FeoB (2, 3). The presence of these fusion proteins in bacterial genomes strongly suggests that FeoA and FeoB are meant to interact and to work in concert with one another. However, these fusions had yet to be studied at the protein level, representing a clear opportunity to probe uniquely into Feo structure and function.

Herein, we provide the first biochemical and biophysical characterization of the soluble domain of the *B. fragilis* FeoAB fusion protein (*Bf*NFeoAB). Using genomic data, we demonstrate that FeoAB fusion proteins are more widespread than initially thought and that these fusions appear to be predominantly found in host-associated bacteria. We subsequently cloned, expressed, and purified *Bf*NFeoAB for X-ray crystallography, small-angle X-ray scattering (SAXS), and hydrogen-deuterium exchange mass spectrometry (HDX-MS). Using these biophysical approaches, we show that *Bf*FeoA bears a conserved SH3-like fold, that apo *Bf*NFeoAB adopts an open, extended conformation in solution, and that interactions of *Bf*FeoA with *Bf*NFeoB occur in a nucleotide-mediated fashion

that occlude essential parts of the G-protein domain. Lastly, we use nuclear magnetic resonance (NMR) spectroscopy to show that the FeoA–NFeoB fusion exhibits exceedingly slow rates of GTP hydrolysis and is not potassium-stimulated. Combined, these data suggest a mechanism in which FeoA interacts with NFeoB in a nucleotide-mediated manner, and we hypothesize this function is to attenuate GTP hydrolysis.

Results

Distribution of FeoAB fusion proteins

Queried nearly a decade ago, a previous study estimated (based on only 33 sequenced bacterial genomes) that \approx 3% of all *feo* operons encode for a fusion of the FeoA protein to the N-terminal, soluble G-protein domain of NFeoB (2, 19). To update the prevalence and distribution of the fusion proteins across bacteria, we leveraged more extensively sequenced genomes and utilized the InterPro database to search for predicted protein architectures containing FeoA (IPR007167). Consistent with the notion that FeoA commonly functions as a single, stand-alone polypeptide, \approx 88% of the *feoA* open reading frames (ORFs) appear to be discontinuous of the *feoB* ORF (25,203 of 28,444 sequences). Interestingly, the encoded FeoA protein is predicted to be fused to another FeoA protein (*i.e.*, FeoA-FeoA or FeoA-FeoA-FeoA) in \approx 3% (791 of 28,444) and \approx 0.1% (29 of 28,444) of gene architectures, respectively. The remaining 2421 genes (*ca.* 8.5% of the sequenced bacterial genomes) are a single, continuous *feoAB* ORF, predicted to encode a single polypeptide in which FeoA is fused to the N-terminal G-protein domain of FeoB, indicating a higher prevalence of this arrangement than initially thought (Fig. 1). Though there is some diversity in the predicted gene architectures among these fusion proteins, a majority (\approx 92%; 2225 sequences) have four predicted domains in total: FeoA, the G-protein domain, the GDI domain, and the TM region (Fig. 1A). Very few ($<$ 3%; 66 sequences) lack a GDI domain. Even more rare, 44 sequences are composed of solely FeoA and the G-protein domain of FeoB, while 31 sequences are composed solely of FeoA and an intact NFeoB (*i.e.*, no TM region; Fig. 1A). However, given the poor conservation of these truncated sequences and their likely lack of function, it is possible that these may be sequencing errors.

We then analyzed the organismal distribution of these fusion sequences to probe their distribution across bacterial phyla (Fig. 1B). FeoAB fusions appear to be predominantly distributed in the *Bacteroidetes* phylum (\approx 44%) and the *Firmicutes* phylum (\approx 39%), which are Gram-negative and Gram-positive bacteria, respectively. These organisms constitute a large portion of the human gut microbiome where they facilitate the breakdown of polysaccharides, such as cellulose and starches, and provide the host with a substantial energy source (37–39). Even fewer sequences are found in *Actinobacteria* (\approx 7%), *Proteobacteria* (\approx 3%), and *Spirochaetes* (\approx 2%), members of which are also found in the human gut microbiome (37, 38). As several of these organisms live in acidic and/or anoxic conditions, it is possible that these bacteria leverage unique

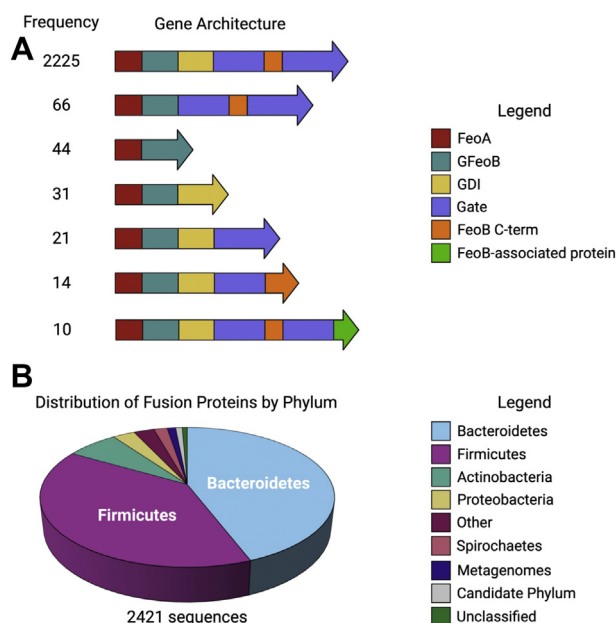


Figure 1. Organization and distribution of FeoAB fusion proteins. A, gene architectures of FeoAB fusion proteins in the InterPro Database as of Feb. 2021. Most FeoAB fusion proteins are predicted to be composed of four domains: FeoA (red), the G-protein domain (teal), the GDI domain (yellow), and the transmembrane region, which comprises the gate domain (purple) and a C-term extension (orange). Very few FeoAB fusion proteins lack the transmembrane region, and these predicted proteins could represent sequencing errors. Though rare, 10 FeoAB fusion proteins are predicted to be fused to an FeoB-associated Cys-rich membrane protein of unknown function (green). B, FeoAB fusion proteins are predominantly distributed in the *Bacteroidetes* (light blue) and *Firmicutes* (purple) phyla. Even fewer are present in *Actinobacteria* (teal), *Proteobacteria* (gold), and *Spirochaetes* (salmon). FeoAB fusion proteins have been discovered in metagenomes (dark blue), uncultured bacteria (gray), and unclassified bacteria (green). Other (dark pink) refers to bacterial phyla with fewer than 10 discovered FeoAB fusions. Figure created with BioRender.

properties of the FeoAB fusion proteins to provide a major portion of the organism's iron stock. Moreover, as it has been suggested that FeoA and FeoB likely interact with one another at the NFeoB domain, we were then motivated to characterize an NFeoAB fusion at the protein level for the first time.

Expression and purification of BfNFeoAB

As these FeoAB fusion proteins have not been characterized *in vitro*, we sought to clone, express, purify, and characterize an NFeoAB fusion to gain insight into FeoA function. Of the >2000 sequences available, we chose *B. fragilis* (a representative of the *Bacteroidetes* phylum), which is a commensal, anaerobic, non-spore-forming bacterium that colonizes the human gut. To investigate the structure and function of one of these N-terminal fusions, the codon-optimized gene corresponding to the N-terminal soluble domain of BfFeoAB (BfNFeoAB; amino acid residues 1–438) (Fig. 2A) was subcloned into a pET-based plasmid and expressed heterologously in *E. coli* with a C-terminal (His)₆ tag for ease of purification. After sonication and lysate clarification, the soluble BfNFeoAB was initially purified *via* immobilized metal affinity chromatography (IMAC). After just one round of column chromatography, large quantities of

significantly pure protein (~80–100 mg/L culture) could be obtained. We then assessed the homogeneity of BfNFeoAB by subsequent size-exclusion chromatography (SEC) on Superdex 200 (Fig. 2B). Interestingly, while a small portion of BfNFeoAB migrated as an apparent trimeric species (estimated <10%; Fig. 2B), the vast majority of the protein (estimated >90%) was monomeric under these conditions (Fig. 2B). This observation contrasts with some theories that NFeoB exists as only a trimeric species (40, 41). Concentration of the monomeric species and subsequent reinjection preserved the monomeric oligomer, indicating that a dynamic equilibrium was not operative on this time scale (several hours; data not shown). We then assessed the purity of our SEC-purified BfNFeoAB by sodium dodecyl sulfate polyacrylamide gel electrophoresis (SDS-PAGE), which migrated similarly to the estimated MW (~53 kDa; Fig. 2C), consistent with our SEC data. This monomeric protein was estimated to be >95% pure and was used for all subsequent biochemical and biophysical analyses.

Crystallization of BfFeoA

Given the high purity and homogeneity of BfNFeoAB, we next sought to crystallize this protein in the apo and nucleotide-bound forms. Despite exhaustive initial crystallization trials in the presence and absence of nucleotides, drops in sparse matrix screens remained mostly clear, even after testing protein concentration, protein state (\pm His tag), nucleotide type, and even nucleotide composition. However, after ~11 months of equilibration, crystals were obtained in ammonium sulfate and dipotassium phosphate that were further optimized by grid screening. After multiple months, medium-sized rectangular crystals appeared that were looped, cryoprotected, and screened for diffraction.

Despite the age of the crystals, diffraction was routinely observed to <2 Å resolution, with our best datasets extending to 1.50 Å (Table S1). After data processing, we initially attempted to phase our data using molecular replacement (MR) of established NFeoB models. However, given the small monoclinic unit cell (C_{121} ; $a = 92.58$ Å; $b = 29.55$ Å, $c = 67.43$ Å; $\alpha = 90^\circ$; $\beta = 128.89^\circ$; and $\gamma = 90^\circ$; Table S1), it was clear that the intact fusion protein could not be present within the lattice with a reasonable solvent content. Under this assumption, we were then able to phase our data by MR using *Clostridium thermocellum* FeoA (PDB ID 2K5L) as an input search model. Initial refinement revealed the presence of two molecules of only the FeoA domain (BfFeoA) in the asymmetric unit (ASU). After iterative rounds of rebuilding and refinement, our BfFeoA model converged with $R_w = 0.192$ and $R_f = 0.236$ (Table S1).

Our crystal structure of BfFeoA comprises residues 1 to 74 of the BfNFeoAB polypeptide (PDB ID 7R7B). As visible in Figure 3A, BfFeoA adopts the β -barrel, SRC Homology 3 (SH3-like) fold that has been observed for other FeoA proteins (19, 20, 42). The β -barrel is composed of five β -strands, while two α -helices make up the clamp region of BfFeoA, which comprises a series of hydrophobic residues (Phe²³, Ile²⁷, Met³⁰,

Characterization of *B. fragilis* NFeoAB

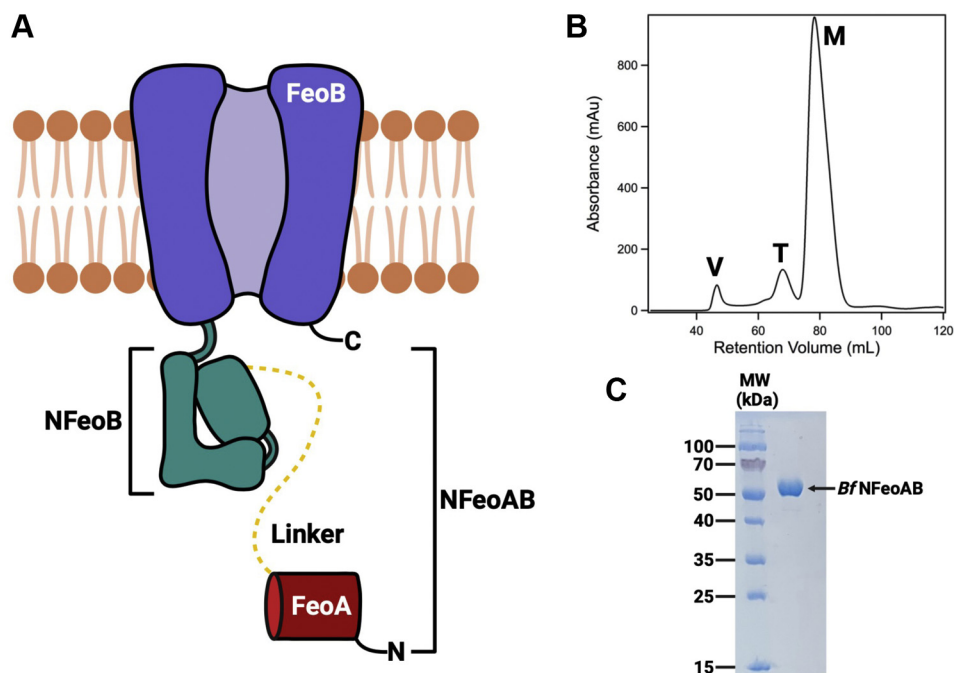


Figure 2. Predicted domain topology of the *BfNFeoAB* construct used in this work and its purification. *A*, cartoon representation of the FeoAB fusion protein from *Bacteroides fragilis*. The FeoA protein (red) is covalently tethered to NFeoB (*teal*) through the G-protein domain by a predicted 44-amino acid linker region (dashed yellow line). The soluble NFeoAB domain is tethered to the transmembrane region of FeoB (purple). Labels 'N' and 'C' refer to the N- and C-termini, respectively. *B*, SEC purification of *BfNFeoAB* on a 120 ml Superdex 200 column. The majority of *BfNFeoAB* is monomeric (≈ 80 ml retention volume; 'M'), while no more than 10% of *BfNFeoAB* is either trimeric (≈ 70 ml retention volume; 'T') or aggregated (≈ 45 ml retention volume; 'V'). *C*, based on SDS-PAGE, *BfNFeoAB* is estimated to be $>95\%$ pure after SEC in panel *B*. Figure created with BioRender.

Ile⁵⁹, and Leu⁶¹) that we have hypothesized to be important for mediating FeoA–NFeoB interactions (Fig. 3B) (20). An additional 3_{10} -helix at the beginning of the N-terminus contacts both the final α -helix and β -strand that feed out of and into the hydrophobic clamp, respectively. Residues comprising both the linker region between FeoA and NFeoB (Fig. 1A) are

completely absent from the structure, likely a result of proteolytic degradation in the crystallization drop over time. While sequence analysis of the FeoA polypeptide does not suggest this is a common proteolytic site, the new C-terminus created after proteolysis is unambiguously present in the electron density (Fig. S1). Although not what we initially set

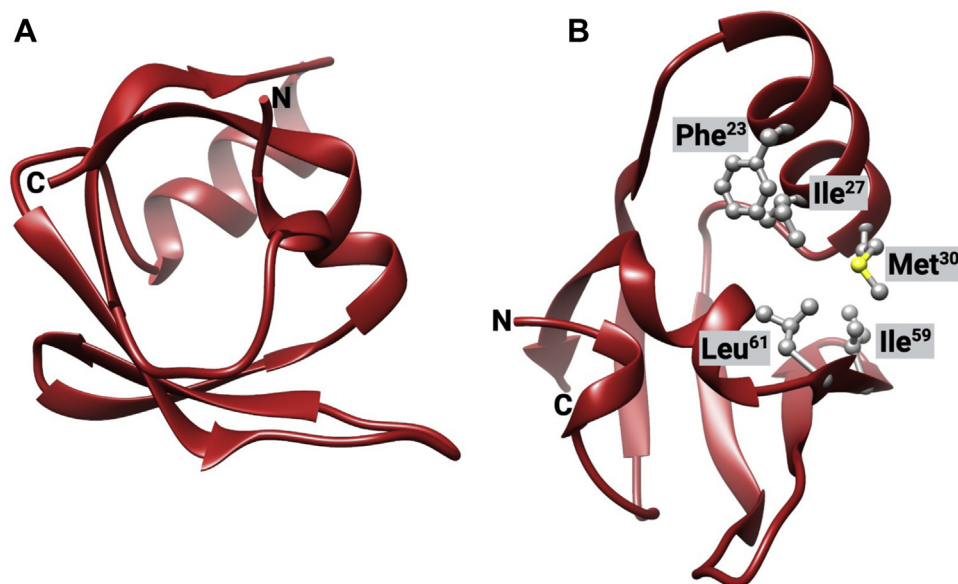


Figure 3. Crystal structure of *BfFeoA*. *A*, similar to other FeoA proteins structurally characterized, *BfFeoA* adopts an SH3-like fold, which is characterized by a small β -barrel. *B*, like observed in the structure of *KpFeoA* (PDB ID 6E55), *BfFeoA* contains a "C-shaped" clamp region lined with hydrophobic residues (shown in ball and stick), composed of Phe²³, Ile²⁷, Met³⁰, Ile⁵⁹, and Leu⁶¹. This view represents a 100° rotation about the y-axis and a 40° rotation about the x-axis of panel *A*. Labels 'N' and 'C' refer to the N- and C-termini, respectively. Figure created with BioRender.

out to crystallize, this structure nevertheless represents the first structure of a portion of the *B. fragilis* Feo system.

Homology modeling

Since our crystallization screening only yielded FeoA crystals, we instead turned to homology modeling to predict the structure of the intact, soluble NFeoAB fusion protein from *B. fragilis*. Using homology approaches applied by the Robetta server (43, 44), five models were generated with high confidence. There appeared to be very little difference among the predicted three-dimensional folds of each model, with the exception of the placement of FeoA and the intervening linker region vis-à-vis NFeoB. A representative model is shown in Figure 4A, which is most consistent with our in-solution biophysical data (*vide infra*).

We then compared our homology models of BfNFeoAB to structurally characterized Feo proteins to determine the locations of each domain of BfNFeoAB. As our newly determined FeoA structure was not part of the homology modeling, we first superposed the FeoA portion of our Robetta model (1–73) with our BfFeoA crystal structure to determine how similar the structures are. Both structures aligned well with a root-mean-square deviation (RMSD) of 0.786 Å over 67 C α s that comprise the core SH3-like fold. The largest deviations were found in two loop regions spanning amino acids 18 to 23 and 42 to 50. We then aligned our models with apo EcNFeoB (PDB ID 3I8S, chain A) and were able to define the BfNFeoB region as spanning residues 110 to 447, while the linker region

spans residues 75 to 109 (Fig. 4A). Interestingly, the linker region was modeled as two α -helices connected by a short, unstructured loop in all Robetta-generated models (Fig. 4A), suggesting more structure in the linker than we initially suspected.

We then determined the locations of key G-protein motifs in our BfNFeoAB models using multiple sequence alignments (Fig. S2) and structural comparisons to apo EcNFeoB. Based on these comparisons, we determined that the G1 motif is located at positions 118 to 125 (GNPNCGKT), the G2 motif is located at position 145 (T), the G3 motif is located at positions 164 to 167 (DLPG), the G4 motif is located at positions 224 to 227 (NMYD), and the G5 motif is located at positions 254 to 259 (CKRNIG). BfNFeoAB also contains a PxxP sequence in the G-protein domain, similar to other FeoB proteins. In *E. coli*, this sequence is located at positions 144 to 147, which corresponds to positions 248 to 251 in BfNFeoAB. Additionally, we predict the Switch I region (Fig. 4A, purple) to be located at positions 134 to 150 and the Switch II region (Fig. 4A, orange) to be located at positions 170 to 191. Structural superpositioning, this time with that of the BfNFeoB models and apo EcNFeoB (PDB ID 3I8S, chain A), resulted in an RMSD of 0.966 Å over 170 C α s in the core of the G protein, although notable exceptions are observed in key dynamic regions. The largest deviations were observed from residues 133 to 146 (the Switch I region), residues 154 to 159 (between the G2 and G3 motifs), the G5 motif, and in residues 270 to 323 that are modeled as an additional α -helix and an unstructured loop between the G-protein and the GDI domain in the

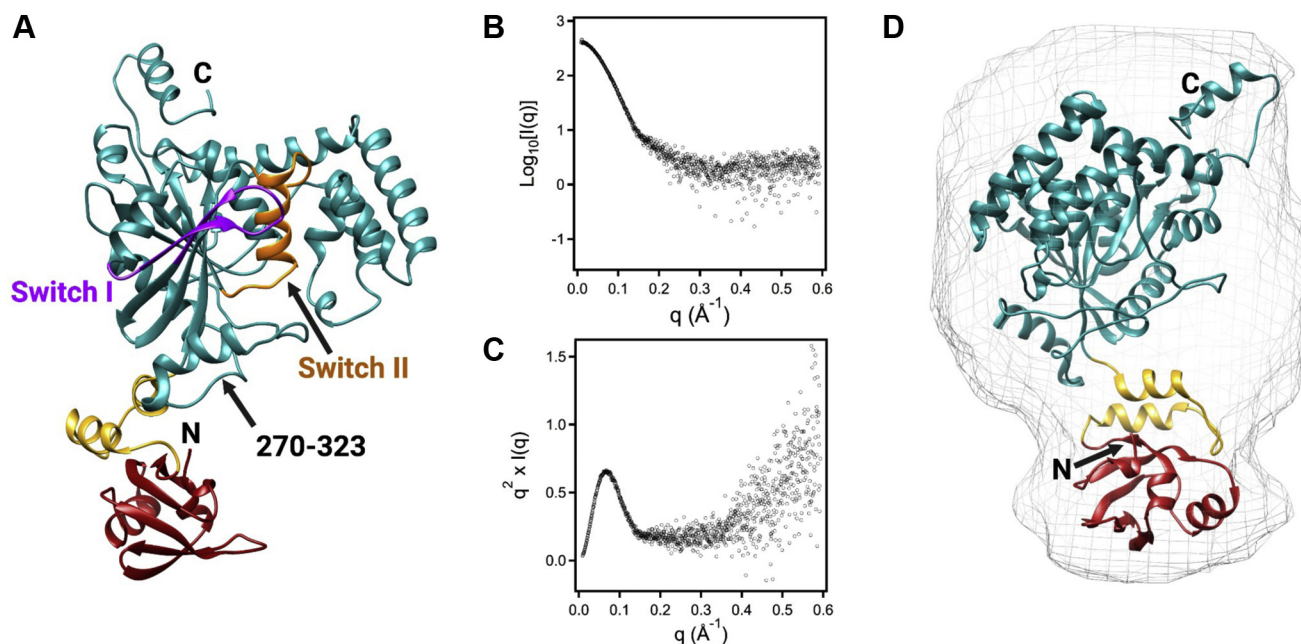


Figure 4. Modeling and SAXS data of apo BfNFeoAB. A, representative Robetta model of apo BfNFeoAB. FeoA (red) is covalently tethered to NFeoB (teal) through a flexible linker region (yellow). Similar to other NFeoB proteins, the Robetta model reveals that BfNFeoAB has both a Switch I region (purple) and a Switch II region (orange). Residues 270 to 323 represent an additional α -helix and unstructured loop not present in other NFeoBs. B, the \log_{10} plot of apo BfNFeoAB SEC-SAXS data indicates that the protein is monodisperse with negligible aggregation. C, the Kratky plot derived from SEC-SAXS data of apo BfNFeoAB is bell-shaped, indicating a well-folded protein. As the curve does not return to 0 at high q values, these data indicate flexibility within the protein. D, overlay of our best-fit Robetta model of apo BfNFeoAB with the *ab initio* envelope (gray mesh) generated from the SEC-SAXS data. The envelope is elongated, and FeoA points away from the G-protein and GDI domains in the apo form. Labels 'N' and 'C' refer to the N- and C-termini, respectively. Figure created with Biorender.

Characterization of *B. fragilis* NFeoAB

*Bf*NFeoAB models but are not present in the apo *Ec*NFeoB structure. Thus, our full-length Robetta models of apo *Bf*NFeoAB are in good agreement with structural data on native and homologous Feo proteins.

Small-angle X-ray scattering

Since we were unable to crystallize intact *Bf*NFeoAB in the presence or absence of nucleotides, we instead used SAXS to determine its solution structure and to compare the experimental solution structure to our Robetta models. Our initial high-throughput (HT) SAXS experiments on apo *Bf*NFeoAB (Fig. S3A) revealed homogenous protein with minimal aggregation in protein samples at low concentrations (Fig. S3B) and suggested an elongated conformation (Fig. S3C), similar to our homology models. This observation was confirmed for apo *Bf*NFeoAB by using SEC-coupled small-angle X-ray scattering (SEC-SAXS), a more robust approach combining gel filtration, multi-angle light scattering, and SAXS (Figs. 4B and S4). The Kratky plot for apo *Bf*NFeoAB (Fig. 4C) exhibits a bell-shaped curve indicating a well-folded protein, with a width that suggests an elongated, nonglobular conformation. In addition, the plot does not converge back to the q axis at high q values, indicating flexibility within the protein. Both analyses agree well with our Robetta models of apo *Bf*NFeoAB, in which *Bf*FeoA is folded separately and disparately of *Bf*NFeoB, and in which the *Bf*FeoA domain appears to sample different conformations dependent on the model. We surmise that this conformational flexibility is a result of the flexibility of the linker region that connects *Bf*FeoA and *Bf*NFeoB.

We then sought to determine the approximate size and molecular envelope of apo *Bf*NFeoAB. Using GNOM from the ATSAS package (45), the best solution for the protein maximal dimension (D_{\max}) of *Bf*NFeoAB was ≈ 80 Å, similar to the longest dimension observed of our elongated Robetta models. GASBOR (46) was then subsequently used to generate 10 independent *ab initio* envelopes (Fig. 4D, gray mesh). The overall shape of the envelope is consistent with an elongated shape, and we were able to identify easily a region in the envelope that strongly resembled the shape of the FeoA domain (Fig. 4D, overlay). To determine which of our Robetta models best fit the *ab initio* envelope, we used SUPCOMB (47), from the ATSAS package, to overlay each model with the envelope (Fig. 4D). In parallel, the online FoXS server (48, 49) was used to determine the fit between the experimental scattering data and the theoretical scattering data calculated for each model. Our best Robetta model, which is shown in Figure 4A, had a χ^2 value of 1.81, indicating a good fit within the *ab initio* envelope.

To determine the effects of nucleotide on the overall structure of *Bf*NFeoAB, we also repeated our HT SAXS experiments in the presence of 5'guanylyl-imidodiphosphate (GMP-PNP) and GDP (Fig. S3A). Though our samples were not as homogenous as our apo protein (Fig. S3B), we noted a marked compaction in the overall structure (Fig. S3C), especially in the presence of GMP-PNP. These observations led us

to hypothesize that FeoA could interact with NFeoB in a nucleotide-dependent manner and could lead to a compaction in structure, and we sought to test this hypothesis and to characterize the sites of this interaction.

Hydrogen–deuterium exchange mass spectrometry

Given our observations that apo *Bf*NFeoAB exists as an elongated conformer in solution and that the conformation of the construct appears to change in the presence of nucleotide, we next sought to map the nucleotide-dependent conformational changes and structural dynamics using HDX-MS. To do so, we incubated apo protein with excess GDP or GMP-PNP (a nonhydrolyzable GTP analog) and compared the uptake of solvent deuterium of these forms of the protein to that of the apo form of the protein at different time points (10 s to 2 h). After incubation, quenching, and digestion to obtain peptides, difference plots reveal the differential percent deuterium uptake in the apo protein compared to the GMP-PNP-bound form (Fig. S5) and the GDP-bound form (Fig. S6). Significant differences in deuterium uptake levels were then mapped onto our *Bf*NFeoAB model in a time-dependent manner for both the GMP-PNP- and GDP-bound forms, and these results reveal major and intriguing differences in the response of the protein based on nucleotide status.

Binding of the nonhydrolyzable GTP analog with GMP-PNP elicits increases in protein protection over a slow time period and throughout the entire protein, suggestive of large changes in conformational dynamics that are consistent with protein compaction and our HT-SAXS data (Fig. S3). In the presence of GMP-PNP, minimal protection from deuterium uptake is observed over the 10-s to 1-min timeframe (Fig. 5A). Significant protection occurs in the GDI domain, in the region containing the additional α -helix and disordered loop (residues 270–323), and in part of the G4 motif (responsible for H-bonding with the guanine nucleotide), which is likely a result of nucleotide recognition. At the 10-min timepoint (Fig. 5B), increased protection is observed in the GDI domain. Moreover, regions of FeoA and the G-protein domain are also protected. These regions include four of the five residues comprising the hydrophobic clamp in FeoA (Ile²⁷, Met³⁰, Ile⁵⁹, and Leu⁶¹), the G1 motif (responsible for binding to the α - and β -phosphate of GTP), the G3 motif (responsible for binding to the γ -phosphate of GTP and Mg²⁺), most of the Switch II region, the region between Switch II and the G4 motif, the PxxP motif (where we posit interactions with the hydrophobic clamp of FeoA occur), and the G5 motif (responsible for H-bonding to the guanine nucleotide). The protection observed at 10 min is consistent with nucleotide binding as most of the G-protein motifs exhibit protection. Interestingly, it is clear that protection of FeoA and the PxxP motif is observed on the same timescale, and these are the few regions that are not directly involved in nucleotide binding, suggesting protein–protein interactions occur in this region. Protection within the G2 motif (responsible for binding to the γ -phosphate of GTP and Mg²⁺) is observed only at the 1-h and 2-h timepoints (Fig. 5C). Under no conditions did we observe significant

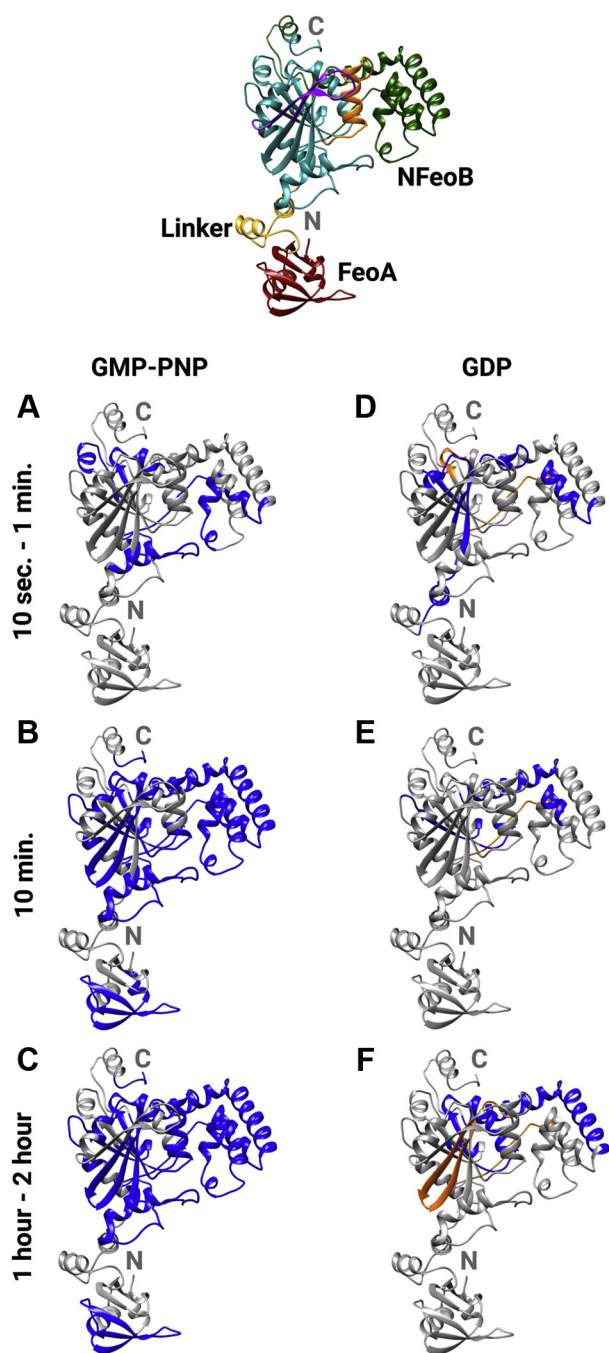


Figure 5. HDX-MS data on *BfNFeoAB* indicate nucleotide- and time-dependent differences in protein protection (blue) and deprotection (orange), which are mapped onto the apo *BfNFeoAB* Robetta model. A, protection from deuterium uptake in the presence of GMP-PNP at both 10 s and 1 min. Most of the protection is observed in the GDI domain. B, continued protection (compaction) is observed of *BfNFeoAB* within 10 min, including the FeoA domain, the G-protein domain, and the GDI domain. C, after 1 to 2 h, most of the GDI domain exhibits protection, as well as the Switch II region, and the key G-protein motifs. D, deprotection of *BfNFeoAB* is only observed in the presence of GDP, beginning as early as 10 s – 1 min, while minimal protection is observed. E, within 10 min, deprotection is observed in the beginning of the GDI domain, while protection within the rest of the protein is limited. F, after 1 to 2 h, deprotection in the Switch I region is observed, as well as protection within the GDI domain. Labels 'N' and 'C' refer to the N- and C-termini, respectively. The top, center panel is color-coded as follows for clarity: FeoA (red), NFeoB (teal), the linker region (yellow), the GDI domain (dark green), the Switch I region (purple), and the Switch II region (orange).

protection within the linker region or within the Switch I region in the presence of GMP-PNP. Notably, across all time points we only observe significant protection and no deprotection in GMP-PNP-bound *BfNFeoAB*, indicating a compaction of structure in this form, consistent with our HT SAXS data.

In contrast, binding of GDP elicits a mixture of protein protection and deprotection and, importantly, does not engage FeoA. In the presence of GDP, we observed minimal protection within the GDI domain over the 10-s to 1-min timeframe (Fig. 5D), similar to the GMP-PNP-bound form. However, we also noted protection within part of the linker region and the beginning of the G-protein domain, motifs G1, G3, and G4, and the beginning of the Switch II region. Unlike in the presence of GMP-PNP, we observed deprotection in the area adjacent to the Switch II region (residues 197–202) and in the random coil that feeds into the beginning of the GDI domain, consistent with our HT-SAXS data indicating the GDP-bound protein is more elongated than the GMP-PNP-bound protein (Fig. S3). This behavior could mimic the protein response post GTP hydrolysis, which would induce conformational changes for GDP release. At 10 min (Fig. 5E), protection is only observed in the region between Switch II and the G4 motif (residues 196–218) and within the PxxP motif. Lastly, by the 1-h and 2-h timepoints (Fig. 5F), deprotection is observed between the G2 and G3 motifs (residues 148–161), while protection is observed in the G3 motif, the beginning of the Switch II region, between Switch II and the G4 motif, between the G4 motif and the PxxP motif, and in the GDI domain. No protection or deprotection of FeoA is observed at any time point, suggesting FeoA does not interact with NFeoB in the GDP-bound state, which could poise the protein for GDP dissociation and/or nucleotide exchange.

Rate of GTP hydrolysis

Finally, as no FeoA–FeoB fusion has been enzymatically characterized, we sought to examine the rate of GTP hydrolysis of *BfNFeoAB* to garner insight into function. Using 1D-³¹P NMR spectroscopy, we performed a full, continuous kinetic characterization of *BfNFeoAB* (Fig. 6). In this assay, signals indicative of GTP (-5.98, -10.91, and -19.39 ppm; corresponding to γ -, α -, and β -phosphates, respectively) slowly reduced in intensity as signals indicative of GDP (-6.08 and -9.92 ppm; corresponding to β - and α -phosphates, respectively) and inorganic phosphate (P_i) (1.91 ppm) increased at the same slow rate. Due to its clear and distinct position, the P_i signal was integrated and plotted with respect to time to assess the rate of hydrolysis. Consistent with findings reported previously by Lau et al (19), no auto-hydrolysis of GTP was observed under these conditions, and *BfNFeoAB* exhibited remarkably slow GTP hydrolysis (k_{cat}^{GTP} (0.71 ± 0.09) $\times 10^{-3}$ s⁻¹) (Fig. 6 and Table 1). As some NFeoBs are not strictly GTPases but, instead, are proposed NTPases (22, 23), we also tested for ATPase activity but did not observe any protein-dependent ATP hydrolysis (data not shown). Interestingly,

Characterization of *B. fragilis* NFeoAB

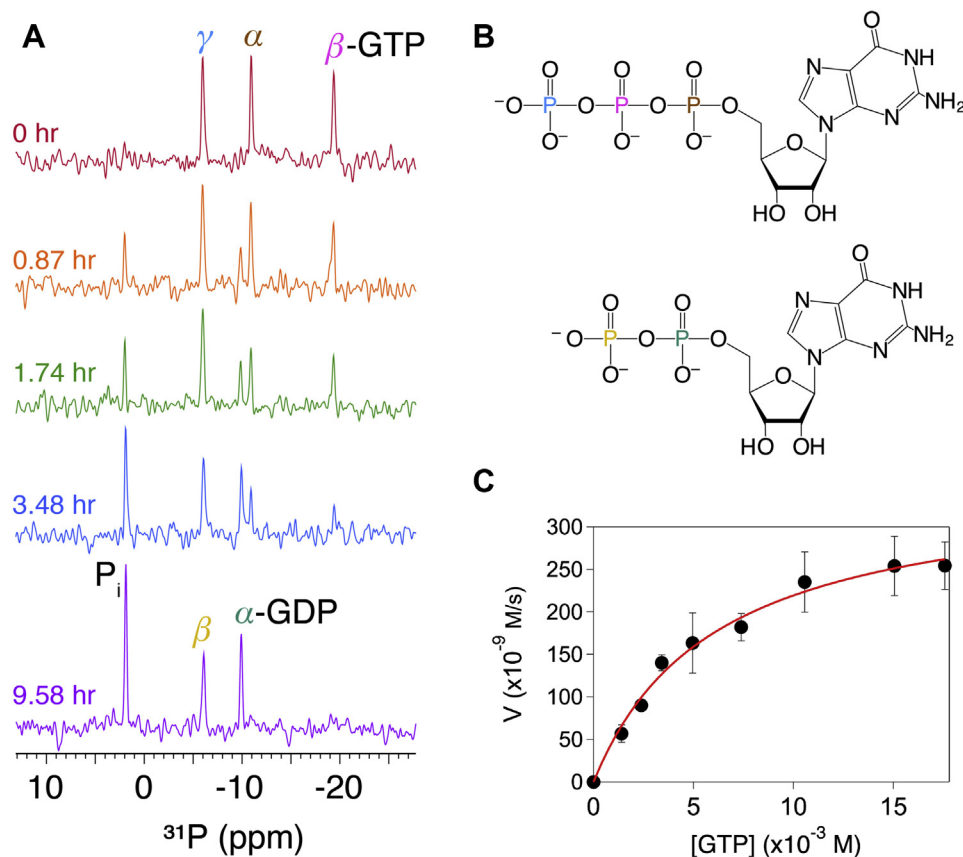


Figure 6. Characterization of the GTPase activity of *BfNFeoAB* by nuclear magnetic resonance (NMR) spectroscopy indicates that nucleotide hydrolysis is exceedingly and notably slow. *A*, exemplar of the 1D- ^{31}P NMR data used to determine the kinetics of 500 μM *BfNFeoAB* in the presence of 5 mM GTP at 310 K. There is progressive reduction in the intensity of α -, β -, and γ -GTP phosphate chemical shifts (brown, magenta, and blue, respectively) until GTP is completely hydrolyzed to GDP (α and β in teal and yellow, respectively) and inorganic phosphate (P_i ; black). *B*, structures of GTP and GDP color-coded to correspond to the phosphate chemical shifts in panel *A* and *C*. The Michaelis-Menten profile of *BfNFeoAB*-catalyzed GTP hydrolysis, which demonstrates a maximum velocity (V_{max}) of $0.35 \pm 0.02 \mu\text{M/s}$ and a Michaelis constant (K_M) of $6.1 \pm 0.8 \text{ mM}$.

the rate of *BfNFeoAB*-catalyzed GTP hydrolysis is at least an order of magnitude slower than all other observed NFeoBs, with the exception of *KpNFeoB* (21, 22, 24). However, *KpNFeoB*, a clear outlier, is known to bind its cognate FeoC (50), and we have shown that intact *KpFeoB* can hydrolyze GTP *ca.* $100 \times 10^{-3} \text{ s}^{-1}$ (27). Moreover, many previous studies have reported increased GTPase activity of NFeoB upon

replacement of NaCl with KCl in the reaction mixture (19, 51), and this K^+ -dependent activation was attributed to two conserved Asn residues (51) that are also found in the sequence of *BfNFeoAB* (Fig. S2). Therefore, we sought to test whether K^+ stimulation could alter the rate of *BfNFeoAB*-catalyzed GTP hydrolysis. To determine the influence of K^+ on activity of *BfNFeoAB*, NMR assays were conducted under identical

Table 1

A comparison of the nucleotide-hydrolyzing enzymatic parameters of NFeoB proteins to those of *BfNFeoAB* and *BfNFeoAB-L*

| Protein | Nucleotide specificity ^a | K_M (mM) | | k_{cat} ($\times 10^{-3} \text{ s}^{-1}$) | | Reference |
|---|-------------------------------------|-------------------|-----------------------------------|---|-----------------------------------|------------|
| | | ATP | GTP | ATP | GTP | |
| <i>Bacteroides fragilis</i> NFeoAB | GTPase | – ^b | 6.1 ± 0.8 | – | 0.71 ± 0.09 | This study |
| <i>Bacteroides fragilis</i> NFeoB-L | GTPase | – | 0.93 ± 0.09 | – | 37 ± 25 | This study |
| <i>Bacillus cereus</i> NFeoB | NTPase | 0.477 ± 0.209 | 4.6 ± 2.3 | – | – | (23) |
| <i>Escherichia coli</i> NFeoB | GTPase | – | 0.13 ± 0.048 | – | 1.5 ± 0.17 | (21) |
| <i>Klebsiella pneumoniae</i> NFeoB | GTPase | – | 0.167 | – | 0.52 | (72) |
| <i>Staphylococcus aureus</i> NFeoB | NTPase | 0.378 ± 0.129 | 1.6 ± 0.76 | – | – | (23) |
| <i>Streptococcus mutans</i> NFeoB | NTPase | 0.388 ± 0.105 | 2.3 ± 0.98 | – | – | (23) |
| <i>Streptococcus thermophilus</i> NFeoB | NTPase | – | – | – | 2.3 ± 1.5^c | (51) |
| | | | | | 43 ± 0.3^d | |
| <i>Vibrio cholerae</i> NFeoB | NTPase | 0.28 ± 0.12 | 0.36 ± 0.15^e | 26 ± 4 | 14.6 | (22) |
| | | | 0.66 ± 0.31^e | | 45 ± 19 | (73) |

Bolded values indicate those determined in this study.

^a Nucleotide specificity based on sequence analyses suggesting a conserved Ala and Ser in the G5 imparts NTPase and GTPase activity, respectively (23).

^b Not determined.

^c Data collected in the presence of NaCl.

^d Data collected in the presence of KCl.

^e Data measured in two different studies.

conditions to those previously used (*vide supra*) except that NaCl was replaced by KCl (Fig. S7). The rate of hydrolysis in K^+ and Na^+ were identical, demonstrating that *BfNFeoAB* GTP hydrolysis is not activated in the presence of K^+ , like many NFeoBs. Thus, *BfNFeoAB* hydrolyzes GTP remarkably slowly, and access to the key Asn residue responsible for potassium stimulation is likely blocked from solvent. Given our findings that the binding of GTP analogs induces interactions between FeoA and NFeoB, we hypothesize that the presence of FeoA reduces the rate of GTP hydrolysis by protein–protein interactions that result in either direct or indirect occlusion of the nucleotide triphosphate.

Expression, purification, and GTPase activity of *BfNFeoB* and *BfNFeoB-L*

To probe further the function of FeoA in the NFeoAB fusion protein, we designed, expressed, and purified 2 *B. fragilis* constructs in which the FeoA domain has been deleted. Our initial *BfNFeoB* construct we designed lacked both FeoA and the linker region but bore an additional C-terminal (His)₆-affinity tag and tobacco etch virus (TEV) protease cleavage site; however, despite multiple expression conditions tested, this construct was only produced in inclusion bodies. Upon multiple refolding efforts, the protein failed to refold as a stable, soluble protein (data not shown), indicating an important role for either FeoA or the linker region in proper folding of the soluble domain.

Therefore, we designed a second construct encoding for the linker region in addition to NFeoB (residues 79–438 of *BfFeoAB*; Fig. S8A) with an additional C-terminal (His)₆-affinity tag and TEV protease cleavage site (*BfNFeoB-L*). *BfNFeoB-L* could be overproduced in *E. coli* and purified using IMAC to a yield of ≈ 130 mg/L culture. To verify that the protein did not aggregate, we then tested the homogeneity of *BfNFeoB-L* via gel filtration and found that, similar to *BfNFeoAB*, *BfNFeoB-L* is highly pure (Fig. S8B) and exists predominantly (>90%) monomeric in solution, indicating that the FeoA domain is not important for oligomerization under these conditions (data not shown).

Lastly, we assessed the GTPase activity of our new, truncated *BfNFeoB-L* construct. As previous optimal conditions had been determined using NMR, we then applied these criteria to the colorimetric malachite green assay, which has been adapted to be rapid and high-throughput. Importantly, in the absence of *BfFeoA*, we found that the protein hydrolyzes GTP at a rate of ≈ 0.04 s⁻¹ (0.037 s⁻¹ \pm 0.025 s⁻¹) and we measured K_M to be 0.93 ± 0.09 mM (Table 1). These data reveal an approximate 50-fold increase in the rate of GTP hydrolysis when FeoA is deleted from *BfNFeoAB*, confirming our hypothesis that FeoA attenuates the rate of GTP hydrolysis and supporting the model that FeoB functions as a GTP-gated channel for Fe²⁺ transport.

Discussion

The function of FeoA vis-à-vis FeoB has garnered considerable debate and yet failed to reach a consensus.

Given its conserved SH3-like fold (19, 20, 42), which typically mediates protein–protein interactions in other systems, our laboratory and others have speculated that FeoA may interact with FeoB to alter function. In support of this notion, *in vivo* studies have demonstrated the ability of FeoA to interact with FeoB in stand-alone tripartite systems (52–54). However, when probed at the *in vitro* level, at least two studies have examined the role of FeoA and its effect on FeoB-catalyzed GTP hydrolysis in stand-alone tripartite systems (19, 22), but virtually no effect was noted. It is possible that, in these systems, the lack of a membrane and/or the inability to reconstitute the correct multicomponent protein system may have shrouded FeoA function. To circumvent this problem, we sought to probe the role of FeoA by taking advantage of a system that exists as a naturally occurring fusion.

We used multiple approaches to characterize a naturally occurring FeoA–FeoB fusion for the first time, with our first focus on structural determination. To decide which fusion protein to target, we undertook a bioinformatics approach, which revealed that these fusions are more widespread in bacteria than previously thought and that the FeoA–FeoB fusion from *B. fragilis* would be a good representative target. After cloning, expression, and purification, this protein was used for crystallization, SEC-SAXS, HDX-MS, and enzymatic assays. As there has been much debate over the oligomeric state of NFeoB/FeoB (whether monomer or trimer) (27, 40, 41, 50, 54–57), it is worth noting that in our hands, *BfNFeoAB* exists predominantly as a monomer (SEC-SAXS–calculated MW: 48.4 kDa \pm 0.7 kDa) in solution at both high and low protein concentrations, though a small amount (estimated <10%) exists as a trimer that is not in dynamic equilibrium with its monomeric form. Nevertheless, we tried to crystallize both, but despite exhaustive crystallization trials, we were only able to crystallize the FeoA domain of this protein. The overall structure of *BfFeoA* (Fig. 3) is similar to other FeoA proteins that have been determined by NMR or X-ray crystallography (19, 20), including the hydrophobic cleft putatively involved in protein–protein interactions, suggesting that the FeoA domain in an FeoAB fusion may function similarly to stand-alone FeoA proteins.

In the absence of a crystal structure of the intact *BfNFeoAB*, we turned to Robetta to generate homology models of our protein (Fig. 4A). In these models, FeoA appears to sample several different conformations, and this flexibility likely explains our difficulty in crystallizing the intact protein. However, this flexibility is undoubtedly linked to function, and we hypothesized interactions of FeoA and NFeoB could be nucleotide mediated. To investigate nucleotide-mediated conformational changes in *BfNFeoAB*, we utilized SEC-SAXS and HDX-MS. Our SEC-SAXS data allowed us to determine the overall low-resolution structure of apo *BfNFeoAB* in solution (Fig. 4), which matches our best-fit Robetta model, both of which indicate the FeoA and NFeoB do not interact in the absence of nucleotide. However, HT-SAXS data strongly suggested a nucleotide-mediated interaction, which we probed with HDX-MS.

Characterization of *B. fragilis* NFeoAB

Our HDX-MS experiments clearly indicated nucleotide-mediated changes in *Bf*NFeoAB that are distinct based on whether nucleotide is intact (GMP-PNP) or hydrolyzed (GDP) and provide insight into the solution behavior of the fusion protein in response to the nucleotide. In both the presence of GMP-PNP and GDP, protection occurs as early as 10 s and 1 min, predominantly in the GDI domain. We posit that this could transduce a signal to the TM region of FeoB and such a signal could “turn on” Fe²⁺ transport (Fig. 7). It is only in the presence of GMP-PNP that we observe protection within FeoA, most of the G-protein motifs, and the PxxP epitope. This behavior indicates that GMP-PNP (a proxy for GTP) binding induces structural and dynamic changes that, together with our SAXS data showing GMP-PNP-dependent compaction, indicate an FeoA–NFeoB interaction. In contrast, the effect of GDP on protection and deprotection in *Bf*NFeoAB is not nearly as dramatic. Similar to the binding of GMP-PNP, the binding of GDP initiates protection of the GDI domain, and we posit that this protein movement transduces a signal to the TM region of FeoB to “turn off” Fe²⁺ transport (Fig. 7). The deprotection observed in the Switch I region in the presence of GDP could also be involved in the release of hydrolyzed nucleotide. Our data do suggest dynamic behavior in the Switch I/II regions, which could have downstream effects on both nucleotide binding and release, consistent with several NFeoB crystal structures (57–59).

In combination with our biophysical analyses and our enzymatic data, we believe these results have strong implications for the function of FeoA. The rate of GTPase activity

of *Bf*NFeoAB and its affinity for GTP (assuming $K_M \sim K_d$) are significantly lower than that of other NFeoBs (Table 1). We believe this phenomenon is explained by the role of FeoA rather than the lack of additional stimulatory factors. First, this and other fusion proteins do not contain an additional ORF in their operons encoding for FeoC, unlike the tripartite Feo systems. Second, neither the use of other nucleotides nor the presence of K⁺ elicits increased hydrolysis rates comparable to other NFeoBs. Third, our HDX-MS data show significant protection of FeoA and the PxxP motif of NFeoB, in addition to expected regions within the nucleotide-binding site, indicating operative protein–protein interactions are occurring. Fourth, we found that our *Bf*NFeoB-L construct in which FeoA was deleted could hydrolyze GTP significantly faster than the intact *Bf*NFeoAB protein with a tighter GTP binding (again assuming $K_M \sim K_d$). Taken together, these findings support our hypothesis that FeoA may regulate the rate of GTP hydrolysis *via* interaction with NFeoB in a nucleotide-dependent manner, which likely controls iron transport across the membrane (Fig. 7). In particular, FeoA may function to slow GTP hydrolysis to keep the transporter “turned on” in a manner similar to eukaryotic GPCRs. These results have *in vivo* implications as studies have shown Fe²⁺ transport to be dependent on GTP hydrolysis (21, 24). After sufficient intracellular iron is then accumulated, an unknown downstream signal could dislodge FeoA from NFeoB to then “turn off” the transporter (Fig. 7). If operative, these protein–protein interactions could be targeted for therapeutic developments to treat infections. For example, multiple organisms such as *B. fragilis* are commensal and colonize the human gut, but if they enter an environment outside of the gastrointestinal tract, they can cause bacteremia, which is becoming increasingly resistant to antibiotic treatments (39). The targeting of FeoA–NFeoB interactions could represent one way to treat these infections by starving the bacterium of this source of iron. However, future work on the intact membrane protein is necessary to probe this hypothesis further.

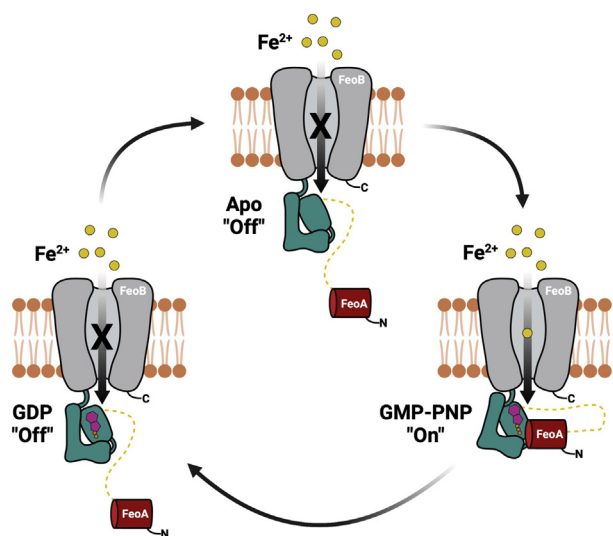


Figure 7. A model of the proposed FeoA-based regulatory function on iron transport of *Bf*FeoAB. In the absence of nucleotide (apo; top), FeoA (red) does not interact with NFeoB (teal), thus transport of Fe²⁺ (yellow) through the transmembrane domain (gray) is in an “off” state. Binding of GMP-PNP (magenta and orange; right), a GTP-analog, to NFeoB induces protein–protein interactions between NFeoB and FeoA. We posit that this GMP-PNP-bound state sends a signal to the transmembrane region to “turn on” Fe²⁺ transport. GDP binding to NFeoB (magenta and orange; left) transduces a signal the transmembrane domain to “turn off” Fe²⁺ transport before dissociation of FeoA–NFeoB interactions, loss of GDP, and a return of the transporter to the apo state.

Experimental procedures

Materials

The codon-optimized gene encoding for the N-terminal soluble domain of *B. fragilis* FeoAB (*Bf*NFeoAB; Uniprot identifier A0A0K6BRR9) was commercially synthesized by GenScript. The pET-21a(+) expression plasmid was purchased from EMD-MilliporeSigma. A C43 (DE3) *E. coli* expression cell line carrying a deletion of *acrB*, an endogenous *E. coli* multidrug exporter (C43 (DE3) Δ *acrB*), was provided by Prof. Edward Yu (Case Western Reserve University). Ampicillin and isopropyl β -D-l-thiogalactopyranoside (IPTG) were purchased from RPI and used as received. Additional materials for cellular growth, protein expression, and protein purification were purchased from MilliporeSigma, VWR, and/or Fisher Scientific and used as received. Sparse-matrix crystallization screens were purchased from Hampton, stored at 4 °C, and allowed to equilibrate at room temperature before use. GTP,

GDP, and GMP-PNP were purchased from MilliporeSigma, stored at $-20\text{ }^{\circ}\text{C}$, and used as received. D_2O was purchased from MilliporeSigma and used as received.

Bioinformatics

FeoA proteins existing as naturally occurring fusions were identified by searching the InterPro Database (accessed February 2021) for all domain architectures containing the FeoA protein (InterPro ID: IPR007167) fused to the G-protein domain of FeoB (InterPro ID: IPR030389). FeoA-like proteins fused to DtxR-type helix-turn-helix domains (InterPro ID: IPR022687), iron-dependent repressors, metal-binding and dimerization domains (InterPro ID: IPR001367), and/or other non-Feo-related proteins were manually removed from the data. The resulting FeoA-containing domain architectures were downloaded from the InterPro database and analyzed. Hierarchical taxonomic information was extracted directly from the truncated database. Multiple sequence alignments were performed using ClustalW (60) and visualized in the JalView suite (version 2.11.1.4 (61)). To determine portions of the FeoAB sequences that belong to cytosolic or membrane domains, the TM helix prediction server (TMHMM, version 2.0) (62) was used.

Cloning, expression, and purification of BfNFeoAB

The presence of the FeoA protein fused to the N-terminal soluble domain of *B. fragilis* (BfNFeoAB) was identified from the full-length FeoAB protein sequence (Uniprot identifier A0A0K6BRR9). Using TMHMM, version 2.0 (62), amino acid residues 1 to 438 were determined to comprise the extent of the cytosolic, soluble fusion domain. The codon-optimized gene encoding for these residues plus an engineered DNA sequence encoding for a C-terminal TEV-protease cleavage site (ENLYFQS) was synthesized by GenScript. This gene was then subcloned into the ampicillin-resistant, IPTG-inducible pET-21a(+) expression plasmid using the NdeI and XhoI restriction sites, encoding for a C-terminal (His)₆-affinity tag used for affinity purification. This expression plasmid bearing BfNFeoAB was subsequently transformed into chemically competent C43 (DE3) Δ acrB *E. coli* expression cells, plated on Luria-Bertani (LB) agar plates containing ampicillin (final concentration of 100 $\mu\text{g}/\text{ml}$) and incubated overnight at $37\text{ }^{\circ}\text{C}$.

Single colonies obtained from these plates were then used to inoculate 100 ml of LB media containing ampicillin (final concentration of 100 $\mu\text{g}/\text{ml}$). This preculture was grown overnight at $37\text{ }^{\circ}\text{C}$ with shaking of 200 RPM and subsequently used to inoculate 12 baffled flasks each containing 1 L of sterile LB media and supplemented with sterile ampicillin (final concentration of 100 $\mu\text{g}/\text{ml}$). These large-scale cultures were grown at $37\text{ }^{\circ}\text{C}$ with shaking of 200 RPM until the A_{600} was ≈ 0.6 to 0.8 . Cultures were then cold shocked for 2 h at $4\text{ }^{\circ}\text{C}$, and protein expression was induced by the addition of sterile IPTG to a final concentration of 1 mM. Flasks were then incubated overnight at $18\text{ }^{\circ}\text{C}$ with shaking of 200 RPM. Cells were harvested after ≈ 16 to 18 h by centrifugation at

4800g for 10 min at $4\text{ }^{\circ}\text{C}$. Cell pellets were resuspended in resuspension buffer (50 mM Tris, pH 7.5, 300 mM NaCl, and 5% (v/v) glycerol), then flash-frozen in $\text{N}_2(\text{l})$, and stored at $-80\text{ }^{\circ}\text{C}$.

To initiate the purification of BfNFeoAB, cells were thawed and homogenized and solid phenylmethylsulfonyl fluoride (50–100 mg) was added prior to cell sonication at $4\text{ }^{\circ}\text{C}$ on a Q700 ultrasonic cell disruptor (QSonica) at an amplitude of 80%, 30 s pulse on, 30 s pulse off for 12 min. The cellular lysate was then clarified by ultracentrifugation at 163,000g at $4\text{ }^{\circ}\text{C}$ for 1 h, and the supernatant was applied to a 5-ml IMAC HisTrap HP column (Cytiva) charged with Ni^{2+} and pre-equilibrated at $4\text{ }^{\circ}\text{C}$ with 5 column volumes (CVs) of wash buffer (50 mM Tris, pH 8.0, 300 mM NaCl, 5% (v/v) glycerol, 1 mM tris(2-carboxyethyl)phosphine [TCEP] HCl) with an additional 21 mM imidazole. The column was then washed with an additional 8 CVs of wash buffer with an additional 21 mM imidazole followed by a wash with 16 CVs of wash buffer with an additional 50 mM imidazole. Protein was eluted from the column with elution buffer (50 mM Tris, pH 8.0, 300 mM NaCl, 5% (v/v) glycerol, 1 mM TCEP, 150 mM imidazole). Fractions containing eluted BfNFeoAB were concentrated at $4\text{ }^{\circ}\text{C}$ using a 15-ml Amicon 3-kDa molecular-weight cutoff (MWCO) spin concentrator (Millipore). Concentrated protein was then further purified by size exclusion chromatography (SEC) on a 120-ml Superdex 200 column (Cytiva) equilibrated with SEC buffer (25 mM Tris, pH 7.5, 300 mM NaCl, 2% (v/v) glycerol, 1 mM TCEP) operating at $4\text{ }^{\circ}\text{C}$. Fractions containing monomeric BfNFeoAB were then concentrated at $4\text{ }^{\circ}\text{C}$ using a 4-ml Amicon 3-kDa MWCO spin concentrator. Protein concentration and purity were determined using the Lowry assay and 15% SDS-PAGE analysis.

The cloning, expression, and purification of BfNFeoB (residues 118–438) and BfNFeoB-L (residues 79–438) were performed in a similar manner to BfNFeoAB with the following slight modifications. After subcloning of BfNFeoB into pET-21a(+), the expression plasmid was then subcloned into electrocompetent BL21 (DE3), C41 (DE3), and C43 (DE3) *E. coli* expression cell lines independently. After subcloning of BfNFeoB-L into pET-21a(+), the expression plasmid was then transformed into an electrocompetent BL21 (DE3) *E. coli* expression cell line. Inclusion bodies (IBs) of BfNFeoB were isolated and refolded based on the protocol outlined in the study by Smith et al (63). BfNFeoB-L was purified identically to BfNFeoAB with the following exception: instead of a 120-ml Superdex 200 column (Cytiva), SEC analyses were performed using a 24-ml Superdex 200 column (Cytiva).

Crystallization, data reduction, and structural determination

SEC-purified BfNFeoAB was concentrated to $\approx 20\text{ mg}/\text{ml}$ and screened for crystallization at room temperature using the vapor diffusion method in 96-well sitting drop trays using commercially available crystallization screens. Initial crystals were obtained in 0.2 M dipotassium phosphate and 2.2 M ammonium sulfate. These crystals were optimized by grid screening in 24-well sitting drop trays at room temperature

Characterization of *B. fragilis* NFeoAB

using the vapor diffusion method. Medium-sized rectangular, crystals appeared in several wells after ≈ 11 months. Crystals were harvested; cryoprotected for ≈ 1 s in a drop containing 1 M ammonium sulfate, 0.1 M dipotassium phosphate and 25% (v/v) glycerol; and frozen on $N_2(l)$. Diffraction data were collected at the Advanced Photon Source (APS), Argonne National laboratory on LS-CAT beamline 21-ID-G. Data were automatically processed using Xia2 (64). Phasing was achieved by MR using Phenix Phaser (65) with *C. thermocellum* FeoA (PDB ID: 2K5L) as an input search model. After an initial MR solution was identified, further model building was accomplished using Phenix AutoBuild (65). Iterative rounds of manual model building and refinement were accomplished in Coot (66) and Phenix Refine (65), respectively, until model convergence. The final model consists of residues 1 to 74 of the FeoA portion of *BfNFeoAB*. This structure has been deposited in the Protein Data Bank (PDB ID: 7R7B). Data collection and refinement statistics are provided in SI Table 1.

Homology modeling

The structural prediction of apo *BfNFeoAB* was determined using comparative modeling, a method used for targets with homologs in the PDB, via the Robetta online server (43, 44). Five structures of *BfNFeoAB* were generated using comparative modeling, each with high confidence. Each model was tested for its agreement to the experimentally determined structure of *BfFeoA* (*vide supra*) and for its fit into the *ab initio* generated molecular envelope that was created from SEC-coupled SAXS data (*vide infra*).

Small-angle X-ray scattering

High-throughput (HT) and SEC-SAXS data were collected at the Advanced Light Source (ALS), Lawrence Berkeley National Laboratory, on the SIBYLS beamline 12.3.1. A suite of samples each containing 60 μ l of *BfNFeoAB* at concentrations ranging from 4 to 6 mg/ml were screened after passage along a PROTEIN KW-803 column equilibrated with SAXS buffer (25 mM Tris, pH 7.5, 150 mM NaCl, 2% (v/v) glycerol, 1 mM TCEP HCl) using an autosampler. Eluent was split 2:1 between the X-ray synchrotron radiation source (SAXS) and a series of four inline analytical instruments: 1) Agilent 1260 series multiple wavelength detector (MWD); 2) Wyatt Dawn Helos multi-angle light scattering detector; 3) Wyatt DynaPro Titan quasi-elastic light scattering detector; and 4) Wyatt Optilab rEX refractometer. Samples were examined with $\lambda = 1.03$ Å incident light at a sample-to-detector distance of 1.5 m resulting in scattering vectors, q , ranging from 0.01 Å $^{-1}$ to 0.5 Å $^{-1}$ where the scattering vector is defined as $q = 4\pi \sin\theta/\lambda$ and 2θ is the measured scattering angle. Data were collected in 3-s exposures over the course of 40 min. SEC-SAXS chromatograms were generated, and initial SAXS curves were analyzed using SCATTER (67, 68). Additionally, UV, multiangle light scattering, quasi-elastic light scattering, and differential refractive index data were collected and analyzed.

Scattering curves were analyzed using SCATTER (67, 68) and GNOM (45) to generate Guinier and Kratky plots and to determine the radius of gyration (R_g) and the maximum particle dimension (D_{max}). *Ab initio* molecular envelopes were generated using GASBOR (46) and averaged with DAMAVER (69) from the ATSAS package and were displayed using Mac PyMOL (version 2.4.1) and UCSF Chimera. *BfNFeoAB* Robetta models were overlaid with SUPCOMB (47), also part of the ATSAS package and displayed using Mac PyMOL (version 2.4.1). The online Fast SAXS Profile Computation with Debye Formula (FoXS) (48, 49) server was used to determine which Robetta model (*vide supra*) best fit the generated *ab initio* envelopes.

Hydrogen–deuterium exchange coupled to mass spectrometry

To begin, undeuterated controls were performed for peptide identification to obtain a sequence coverage map for *BfNFeoAB*. The experimental workflow is as follows: 2 μ l of 20 μ M *BfNFeoAB* in 25 mM Tris pH 7.5, 300 mM NaCl, 2% (v/v) glycerol, 1 mM TCEP was diluted with 98 μ l of ice-cold quench (100 mM glycine pH 2.5, 1 M guanidine-HCl, 5 mM TCEP). After 1 min, 100 μ l of dilution was injected into a Waters HDX nanoACQUITY UPLC (Waters, Milford, MA) with in-line protease XIII/pepsin digestion (NovoBioAssays LLC). Peptic fragments were trapped on an ACQUITY UPLC BEH C18 peptide trap and separated on an ACQUITY UPLC BEH C18 column. A 7-min, 5% to 35% acetonitrile in 0.1% formic acid gradient was used to elute the peptides directly into a Waters Synapt G2-Si mass spectrometer (Waters, Milford, MA). MS e data were acquired with a 20- to 30-V ramp trap collision energy (CE) for high energy acquisition of product ions and continuous lock mass (Leucine-Enkephalin) for correction of mass accuracy. Peptides were identified using the ProteinLynx Global Server 3.0.3 (Waters). A filter of 0.3 fragments per residue was applied for peptide processing in the DynamX 3.0 software (Waters).

Hydrogen–deuterium exchange reactions for apo *BfNFeoAB* and the protein in complex with GMP-PNP were performed by manual injections. The same reactions of the apo protein and the protein in complex with GDP were acquired with a LEAP autosampler controlled by the Chronos software. The reaction workflow for both manual and autosampler injections was as follows: 4 μ l of 10 μ M protein in complex with 5 mM GMP-PNP or 5 mM GDP was incubated in 36 μ l of 25 mM Tris in D $_2$ O (99.99%), pD 7.5, 300 mM NaCl, 2% (v/v) glycerol and 1 mM TCEP. The 40- μ l reaction was quenched at various times with 60 μ l of 100 mM glycine pH 2.5, 2.5 M guanidine-HCl and 5 mM TCEP. All the deuteration reactions were carried out at 25 °C at five reaction time points (10 s, 1 min, 10 min, 1 h, and 2 h). Following quenching of the deuterated samples, the 100- μ l quenched reaction was injected and LC/MS acquisition was performed in the same manner as the undeuterated controls. The five deuteration time points were acquired in triplicate. Fully deuterated controls were performed for normalization purposes. The normalized

percent deuterium uptake (%D) for each peptide, at incubation time t , was calculated as described in the equation in the following:

$$\% D = \frac{100 \times (m_t - m_0)}{m_f - m_0}$$

where m_t , m_0 , and m_f are the centroid masses at incubation time t , the undeuterated control, and the fully deuterated control, respectively. The reaction workflow for the fully deuterated controls was as follows: 10 μ l of 60 μ M BfNFeoAB was incubated with 10 μ l of 25 mM Tris pH 7.5, 7.84 M guanidine-HCl, and the protein was incubated overnight. Subsequently, 4 μ l of the unfolding reaction was diluted with 36 μ l of D₂O buffer, pD 7.4, and allowed to deuterate for more than 2 h. The reaction was quenched with 60 μ l of quench buffer and injected, with LC/MS acquisition performed as described earlier. The DynamX 3.0 software was used for spectral curation, centroid calculation, and deuterium uptake analysis of all identified peptides.

GTPase assays

Samples for NMR experiments were prepared in 100 mM Tris, pH 7.5, 300 mM NaCl, 100 mM MgSO₄, 2% (v/v) glycerol, 1 mM TCEP, and 10% D₂O in a 3-mm NMR tube. Experiments in which the contribution of K⁺ was monitored were carried out under the same conditions as outlined earlier except NaCl was replaced by KCl. The GTPase and ATPase activities of \approx 500 μ M BfNFeoAB were monitored by 1D-³¹P NMR spectroscopy at 37 °C using a 500-MHz Bruker DMX spectrometer equipped with a room temperature probe. NMR spectra were collected using 256 scans with a 10- to 30-min delay between acquisitions, and data were processed using dataChord Spectrum Analyst (70). The velocity profiles were based on linear initial rates; to determine Michaelis–Menten kinetics, GTP concentrations were varied from 1.5 mM to 18 mM. Over these substrate concentrations, initial velocity measurements were plotted *versus*. substrate concentration (GTP or ATP) and fitted to the following equation:

$$v = \frac{V_{max}[S]}{K_m + [S]}$$

The GTPase activity of the BfNFeoB-L construct was measured using a modified malachite green assay, described previously (27, 71). Stocks of BfNFeoB-L were diluted to \approx 7 μ M in a malachite green reaction buffer (100 mM Tris, pH 7.5, 3 mM MgCl₂, 100 mM NaCl). Na₂GTP was added to varying concentrations (from 0.15 mM to 2.25 mM) to initiate the reaction, and solution mixtures were incubated at 37 °C with shaking for 0 to 90 min. Aliquots were quenched by the addition of a malachite green working solution (1.05% (w/v) ammonium molybdate tetrahydrate, 0.0338% (w/v) malachite green carbinol, 1.0 M HCl, all final concentrations). A stock of 34% sodium citrate (100 μ l) was added to each quenched reaction mixture. The absorbance of the solution was measured

at 660 nm using a Cary 60 UV-Vis spectrophotometer (Agilent). A standard curve for inorganic phosphate (P_i) was used to calculate the amount of P_i released during the reaction. Background GTP hydrolysis was measured in the same manner but without enzyme, and results were used for data correction.

Data availability

All data are contained within the manuscript, either in the main body or in the Supplemental data submitted with the manuscript, and/or deposited in repositories such as the Protein Data Bank (PDB).

*Supporting information—*BfFeoA data collection and refinement statistics (Table S1)

The 2F_O-F_C electron density map of BfFeoA (Fig. S1)

Partial multiple sequence alignments (MSAs) of the soluble, N-terminal domains of non-fused FeoB proteins and select FeoAB fusion proteins (Fig. S2)

Experimental high-throughput (HT) SAXS data for apo and nucleotide-bound BfNFeoAB (Fig. S3)

SEC-R_g profile for apo BfNFeoAB (Fig. S4)

Difference plots of apo BfNFeoAB percent deuterium uptake (%D_{apo}) minus GMP-PNP-bound BfNFeoAB percent deuterium uptake (%D_{GMP-PNP}) (Fig. S5)

Difference plots of apo BfNFeoAB percent deuterium uptake (%D_{apo}) minus GDP-bound BfNFeoAB percent deuterium uptake (%D_{GDP}) (Fig. S6)

BfNFeoAB GTP hydrolysis in the presence of K⁺ and Na⁺ (Fig. S7)

Cartoon representation and SDS-PAGE analysis of purified BfNFeoB-L (Fig. S8)

This article contains supporting information.

*Author contributions—*A. E. S., J. B. B., J. O. O., and S. M. O' S. investigation; A. E. S., J. B. B., J. O. O., E. D. G., and D. J. D. formal analysis; A. E. S., J. B. B., J. O. O., and S. M. O' S. validation; A. E. S., J. B. B., and J. O. O. writing - original draft; A. E. S., J. B. B., J. O. O., S. M. O' S., E. D. G., D. J. D., and A. T. S. writing - review and editing; A. E. S., J. B. B., J. O. O., and A. T. S. visualization. A. T. S. supervision; A. T. S. funding acquisition; A. T. S. project administration.

*Funding and additional information—*This work was supported by NIH-NIDCR grant R21 DE027803, NIH-NIGMS grant R35 GM133497, in part by NIH-NIGMS grant T32 GM066706 (A. E. S. and J. O. O.), and by the University of Maryland Baltimore, School of Pharmacy Mass Spectrometry Center (SOP1841-IQB2014). This research used resources of the Advanced Photon Source, a U.S. Department of Energy (DOE) Office of Science User Facility operated for the DOE Office of Science by Argonne National Laboratory under Contract No. DE-AC02 to 06CH11357. Use of the LS-CAT Sector 21 was supported by the Michigan Economic Development Corporation and the Michigan Technology Tri-Corridor (Grant 085P1000817). SAXS experiments were conducted at the Advanced Light Source (ALS), a national user facility operated by Lawrence Berkeley National Laboratory on behalf of the Department of Energy, Office of Basic Energy Sciences, through the Integrated Diffraction Analysis Technologies (IDAT) program, supported by the DOE Office of Biological and Environmental Research. Additional support comes from the National Institute of Health project

Characterization of *B. fragilis* NFeoAB

ALS-ENABLE (P30 GM124169) and a High-End Instrumentation Grant S10OD018483. Sequence searches utilized both database and analysis functions of the Universal Protein Resource (UniProt) Knowledgebase and Reference Clusters (<http://www.uniprot.org>) and the National Center for Biotechnology Information (<http://www.ncbi.nlm.nih.gov/>). NMR experiments were carried out at the University of Maryland Baltimore County Molecular Characterization and Analysis Complex.

Conflict of interest—The authors declare that they have no conflicts of interest with the contents of this article.

Abbreviations—The abbreviations used are: GDP, guanosine diphosphate; GMP-PNP, 5'guanylyl-imidodiphosphate; GTP, guanosine triphosphate; IMAC, immobilized metal affinity chromatography; IPTG, isopropyl β -D-l-thiogalactopyranoside; NFeoAB, soluble N-terminal GTP-binding domain of FeoB fused to FeoA; NFeoB, soluble N-terminal GTP-binding domain of FeoB; NMR, nuclear magnetic resonance; RMSD, root-mean-square deviation; SAXS, small-angle X-ray scattering; SDS-PAGE, sodium dodecyl sulfate polyacrylamide gel electrophoresis; SEC, size-exclusion chromatography; SEC-SAXS, SEC-coupled small-angle X-ray scattering; TCEP, tris(2-carboxyethyl)phosphine; TEV, tobacco etch virus; Tris, tris(hydroxymethyl)aminomethane.

References

- Andrews, S. C., Robinson, A. K., and Rodríguez-Quiñones, F. (2003) Bacterial iron homeostasis. *FEMS Microbiol. Rev.* **27**, 215–237
- Lau, C. K., Krewulak, K. D., and Vogel, H. J. (2016) Bacterial ferrous iron transport: The feo system. *FEMS Microbiol. Rev.* **40**, 273–298
- Sestok, A. E., Linkous, R. O., and Smith, A. T. (2018) Toward a mechanistic understanding of Feo-mediated ferrous iron uptake. *Metallomics* **10**, 887–898
- Torrents, E. (2014) Ribonucleotide reductases: Essential enzymes for bacterial life. *Front. Cell Infect. Microbiol.* **4**, 52
- Hu, Y., and Ribbe, M. W. (2015) Nitrogenase and homologs. *J. Biol. Inorg. Chem.* **20**, 435–445
- Brzóska, K., Meczynska, S., and Kruszewski, M. (2006) Iron-sulfur cluster proteins: Electron transfer and beyond. *Acta Biochim. Pol.* **53**, 685–691
- Wittenberg, J. B., Bolognesi, M., Wittenberg, B. A., and Guertin, M. (2002) Truncated hemoglobins: A new family of hemoglobins widely distributed in bacteria, unicellular eukaryotes, and plants. *J. Biol. Chem.* **277**, 871–874
- Krewulak, K. D., and Vogel, H. J. (2008) Structural biology of bacterial iron uptake. *Biochim. Biophys. Acta* **1778**, 1781–1804
- Winterbourn, C. C. (1995) Toxicity of iron and hydrogen peroxide: The Fenton reaction. *Toxicol. Lett.* **82–83**, 969–974
- Chu, B. C., Garcia-Herrero, A., Johanson, T. H., Krewulak, K. D., Lau, C. K., Peacock, R. S., Slavinskaya, Z., and Vogel, H. J. (2010) Siderophore uptake in bacteria and the battle for iron with the host; a bird's eye view. *Biometals* **23**, 601–611
- Ellermann, M., and Arthur, J. C. (2017) Siderophore-mediated iron acquisition and modulation of host-bacterial interactions. *Free Radic. Biol. Med.* **105**, 68–78
- Cain, T. J., and Smith, A. T. (2021) Ferric iron reductases and their contribution to unicellular ferrous iron uptake. *J. Inorg. Biochem.* **218**, 111407
- Cescou, S., Cwerman, H., Létouffé, S., Delepelaire, P., Wandersman, C., and Biville, F. (2007) Heme acquisition by hemophores. *Biometals* **20**, 603–613
- Huang, W., and Wilks, A. (2017) Extracellular heme uptake and the challenge of bacterial cell membranes. *Annu. Rev. Biochem.* **86**, 799–823
- Richard, K. L., Kelley, B. R., and Johnson, J. G. (2019) Heme uptake and utilization by Gram-negative bacterial pathogens. *Front. Cell Infect. Microbiol.* **9**, 81
- Hantke, K. (1987) Ferrous iron transport mutants in *Escherichia coli* K12. *FEMS Microbiol. Lett.* **44**, 53–57
- Kammler, M., Schön, C., and Hantke, K. (1993) Characterization of the ferrous iron uptake system of *Escherichia coli*. *J. Bacteriol.* **175**, 6212–6219
- Hantke, K. (2003) Is the bacterial ferrous iron transporter FeoB a living fossil? *Trends Microbiol.* **11**, 192–195
- Lau, C. K., Ishida, H., Liu, Z., and Vogel, H. J. (2013) Solution structure of *Escherichia coli* FeoA and its potential role in bacterial ferrous iron transport. *J. Bacteriol.* **195**, 46–55
- Linkous, R. O., Sestok, A. E., and Smith, A. T. (2019) The crystal structure of *Klebsiella pneumoniae* FeoA reveals a site for protein-protein interactions. *Proteins* **87**, 897–903
- Marlovits, T. C., Haase, W., Herrmann, C., Aller, S. G., and Unger, V. M. (2002) The membrane protein FeoB contains an intramolecular G protein essential for Fe(II) uptake in bacteria. *Proc. Natl. Acad. Sci. U. S. A.* **99**, 16243–16248
- Shin, M., Mey, A. R., and Payne, S. M. (2019) FeoB contains a dual nucleotide-specific NTPase domain essential for ferrous iron uptake. *Proc. Natl. Acad. Sci. U. S. A.* **116**, 4599–4604
- Shin, M., Park, J., Jin, Y., Kim, I. J., Payne, S. M., and Kim, K. H. (2020) Biochemical characterization of bacterial FeoBs: A perspective on nucleotide specificity. *Arch. Biochem. Biophys.* **685**, 108350
- Eng, E. T., Jalilian, A. R., Spasov, K. A., and Unger, V. M. (2008) Characterization of a novel prokaryotic GDP dissociation inhibitor domain from the G protein coupled membrane protein FeoB. *J. Mol. Biol.* **375**, 1086–1097
- Seyedmohammad, S., Born, D., and Venter, H. (2014) Expression, purification and functional reconstitution of FeoB, the ferrous iron transporter from *Pseudomonas aeruginosa*. *Protein Expr. Purif.* **101**, 138–145
- Hagelueken, G., Duthie, F. G., Florin, N., Schubert, E., and Schiemann, O. (2015) Expression, purification and spin labelling of the ferrous iron transporter FeoB from *Escherichia coli* BL21 for EPR studies. *Protein Expr. Purif.* **114**, 30–36
- Smith, A. T., and Sestok, A. E. (2018) Expression and purification of functionally active ferrous iron transporter FeoB from *Klebsiella pneumoniae*. *Protein Expr. Purif.* **142**, 1–7
- Robey, M., and Cianciotto, N. P. (2002) *Legionella pneumophila* feoAB promotes ferrous iron uptake and intracellular infection. *Infect. Immun.* **70**, 5659–5669
- Naikare, H., Palyada, K., Panciera, R., Marlow, D., and Stintzi, A. (2006) Major role for FeoB in *Campylobacter jejuni* ferrous iron acquisition, gut colonization, and intracellular survival. *Infect. Immun.* **74**, 5433–5444
- Thomas-Charles, C. A., Zheng, H., Palmer, L. E., Mena, P., Thanassi, D. G., and Furie, M. B. (2013) FeoB-mediated uptake of iron by *Francisella tularensis*. *Infect. Immun.* **81**, 2828–2837
- Sabri, M., Caza, M., Proulx, J., Lymberopoulos, M. H., Brée, A., Moulin-Schouleur, M., Curtiss, R., 3rd, and Dozois, C. M. (2008) Contribution of the SitABCD, MntH, and FeoB metal transporters to the virulence of avian pathogenic *Escherichia coli* O78 strain chi7122. *Infect. Immun.* **76**, 601–611
- Runyen-Janecky, L. J., Reeves, S. A., Gonzales, E. G., and Payne, S. M. (2003) Contribution of the *Shigella flexneri* Sit, Iuc, and Feo iron acquisition systems to iron acquisition *in vitro* and in cultured cells. *Infect. Immun.* **71**, 1919–1928
- Aranda, J., Cortés, P., Garrido, M. E., Fittipaldi, N., Llagostera, M., Gottschalk, M., and Barbé, J. (2009) Contribution of the FeoB transporter to *Streptococcus suis* virulence. *Int. Microbiol.* **12**, 137–143
- Dashper, S. G., Butler, C. A., Lissel, J. P., Paolini, R. A., Hoffmann, B., Veith, P. D., O'Brien-Simpson, N. M., Snelgrove, S. L., Tsiros, J. T., and Reynolds, E. C. (2005) A novel *Porphyromonas gingivalis* FeoB plays a role in manganese accumulation. *J. Biol. Chem.* **280**, 28095–28102

35. Veeranagouda, Y., Husain, F., Boente, R., Moore, J., Smith, C. J., Rocha, E. R., Patrick, S., and Wexler, H. M. (2014) Deficiency of the ferrous iron transporter FeoAB is linked with metronidazole resistance in *Bacteroides fragilis*. *J. Antimicrob. Chemother.* **69**, 2634–2643
36. Rocha, E. R., Bergonia, H. A., Gerdes, S., and Jeffrey Smith, C. (2019) *Bacteroides fragilis* requires the ferrous-iron transporter FeoAB and the CobN-like proteins BtuS1 and BtuS2 for assimilation of iron released from heme. *Microbiologyopen* **8**, e00669
37. Bäckhed, F., Ley, R. E., Sonnenburg, J. L., Peterson, D. A., and Gordon, J. I. (2005) Host-bacterial mutualism in the human intestine. *Science* **307**, 1915–1920
38. Ley, R. E., Peterson, D. A., and Gordon, J. I. (2006) Ecological and evolutionary forces shaping microbial diversity in the human intestine. *Cell* **124**, 837–848
39. Wexler, H. M. (2007) Bacteroides: The good, the bad, and the nitty-gritty. *Clin. Microbiol. Rev.* **20**, 593–621
40. Hagelueken, G., Hoffmann, J., Schubert, E., Duthie, F. G., Florin, N., Konrad, L., Imhof, D., Behrmann, E., Morgner, N., and Schiemann, O. (2016) Studies on the X-ray and solution structure of FeoB from *Escherichia coli* BL21. *Biophys. J.* **110**, 2642–2650
41. Seyedmohammad, S., Fuentealba, N. A., Marriott, R. A., Goetze, T. A., Edwardson, J. M., Barrera, N. P., and Venter, H. (2016) Structural model of FeoB, the iron transporter from *Pseudomonas aeruginosa*, predicts a cysteine lined, GTP-gated pore. *Biosci. Rep.* **36**, e00322
42. Su, Y. C., Chin, K. H., Hung, H. C., Shen, G. H., Wang, A. H., and Chou, S. H. (2010) Structure of *Stenotrophomonas maltophilia* FeoA complexed with zinc: A unique prokaryotic SH3-domain protein that possibly acts as a bacterial ferrous iron-transport activating factor. *Acta Crystallogr. Sect. F Struct. Biol. Cryst. Commun.* **66**, 636–642
43. Raman, S., Vernon, R., Thompson, J., Tyka, M., Sadreyev, R., Pei, J., Kim, D., Kellogg, E., DiMaio, F., Lange, O., Kinch, L., Sheffler, W., Kim, B. H., Das, R., Grishin, N. V., et al. (2009) Structure prediction for CASP8 with all-atom refinement using Rosetta. *Proteins* **77**, 89–99
44. Song, Y., DiMaio, F., Wang, R. Y., Kim, D., Miles, C., Brunette, T., Thompson, J., and Baker, D. (2013) High-resolution comparative modeling with RosettaCM. *Structure* **21**, 1735–1742
45. Svergun, D. I. (1992) Determination of the regularization parameter in indirect-transform methods using perceptual criteria. *J. Appl. Crystallogr.* **25**, 495–503
46. Svergun, D. I., Petoukhov, M. V., and Koch, M. H. (2001) Determination of domain structure of proteins from X-ray solution scattering. *Biophys. J.* **80**, 2946–2953
47. Kozin, M. B., and Svergun, D. I. (2001) Automated matching of high- and low-resolution structural models. *J. Appl. Crystallogr.* **34**, 33–41
48. Schneidman-Duhovny, D., Hammel, M., Tainer, J. A., and Sali, A. (2013) Accurate SAXS profile computation and its assessment by contrast variation experiments. *Biophys. J.* **105**, 962–974
49. Schneidman-Duhovny, D., Hammel, M., Tainer, J. A., and Sali, A. (2016) FoXS, FoXSDock and MultiFoXS: Single-state and multi-state structural modeling of proteins and their complexes based on SAXS profiles. *Nucleic Acids Res.* **44**, W424–429
50. Hung, K. W., Tsai, J. Y., Juan, T. H., Hsu, Y. L., Hsiao, C. D., and Huang, T. H. (2012) Crystal structure of the *Klebsiella pneumoniae* NFeoB/FeoC complex and roles of FeoC in regulation of Fe²⁺ transport by the bacterial Feo system. *J. Bacteriol.* **194**, 6518–6526
51. Ash, M. R., Guilfoyle, A., Clarke, R. J., Guss, J. M., Maher, M. J., and Jormakka, M. (2010) Potassium-activated GTPase reaction in the G Protein-coupled ferrous iron transporter B. *J. Biol. Chem.* **285**, 14594–14602
52. Kim, H., Lee, H., and Shin, D. (2012) The FeoA protein is necessary for the FeoB transporter to import ferrous iron. *Biochem. Biophys. Res. Commun.* **423**, 733–738
53. Weaver, E. A., Wyckoff, E. E., Mey, A. R., Morrison, R., and Payne, S. M. (2013) FeoA and FeoC are essential components of the *Vibrio cholerae* ferrous iron uptake system, and FeoC interacts with FeoB. *J. Bacteriol.* **195**, 4826–4835
54. Stevenson, B., Wyckoff, E. E., and Payne, S. M. (2016) *Vibrio cholerae* FeoA, FeoB, and FeoC interact to form a complex. *J. Bacteriol.* **198**, 1160–1170
55. Deshpande, C. N., McGrath, A. P., Font, J., Guilfoyle, A. P., Maher, M. J., and Jormakka, M. (2013) Structure of an atypical FeoB G-domain reveals a putative domain-swapped dimer. *Acta Crystallogr. Sect. F Struct. Biol. Cryst. Commun.* **69**, 399–404
56. Ovchinnikov, S., Park, H., Varghese, N., Huang, P. S., Pavlopoulos, G. A., Kim, D. E., Kamisetty, H., Kyrpides, N. C., and Baker, D. (2017) Protein structure determination using metagenome sequence data. *Science* **355**, 294–298
57. Koster, S., Wehner, M., Herrmann, C., Kuhlbrandt, W., and Yildiz, O. (2009) Structure and function of the FeoB G-domain from *Methanococcus jannaschii*. *J. Mol. Biol.* **392**, 405–419
58. Köster, S., Kuhlbrandt, W., and Yildiz, O. (2009) Purification, crystallization and preliminary X-ray diffraction analysis of the FeoB G domain from *Methanococcus jannaschii*. *Acta Crystallogr. Sect. F Struct. Biol. Cryst. Commun.* **65**, 684–687
59. Ash, M. R., Maher, M. J., Guss, J. M., and Jormakka, M. (2011) The initiation of GTP hydrolysis by the G-domain of FeoB: Insights from a transition-state complex structure. *PLoS One* **6**, e23355
60. Larkin, M. A., Blackshields, G., Brown, N. P., Chenna, R., McGettigan, P. A., McWilliam, H., Valentin, F., Wallace, I. M., Wilm, A., Lopez, R., Thompson, J. D., Gibson, T. J., and Higgins, D. G. (2007) Clustal W and clustal X version 2.0. *Bioinformatics* **23**, 2947–2948
61. Waterhouse, A. M., Procter, J. B., Martin, D. M., Clamp, M., and Barton, G. J. (2009) Jalview Version 2 - a multiple sequence alignment editor and analysis workbench. *Bioinformatics* **25**, 1189–1191
62. Krogh, A., Larsson, B., von Heijne, G., and Sonnhammer, E. L. L. (2001) Predicting transmembrane protein topology with a hidden markov model: Application to complete genomes. *J. Mol. Biol.* **305**, 567–580
63. Smith, S. M., Balasubramanian, R., and Rosenzweig, A. C. (2011) Metal reconstitution of particulate methane monooxygenase and heterologous expression of the pmoB subunit. *Methods Enzymol.* **495**, 195–210
64. Winter, G. (2010) Xia2: An expert system for macromolecular crystallography data reduction. *J. Appl. Crystallogr.* **43**, 186–190
65. Adams, P. D., Afonine, P. V., Bunkóczi, G., Chen, V. B., Davis, I. W., Echols, N., Headd, J. J., Hung, L. W., Kapral, G. J., Grosse-Kunstleve, R. W., McCoy, A. J., Moriarty, N. W., Oeffner, R., Read, R. J., Richardson, D. C., et al. (2010) Phenix: A comprehensive Python-based system for macromolecular structure solution. *Acta Crystallogr. D Biol. Crystallogr.* **66**, 213–221
66. Emsley, P., and Cowtan, K. (2004) Coot: Model-building tools for molecular graphics. *Acta Crystallogr. D Biol. Crystallogr.* **60**, 2126–2132
67. Förster, S., Timmann, A., Konrad, M., Schellbach, C., Meyer, A., Funari, S. S., Mulvaney, P., and Knott, R. (2005) Scattering curves of ordered mesoscopic materials. *J. Phys. Chem. B* **109**, 1347–1360
68. Förster, S., Apostol, L., and Bras, W. (2010) Scatter: Software for the analysis of nano- and mesoscale small-angle scattering. *J. Appl. Crystallogr.* **43**, 639–646
69. Volkov, V. V., and Svergun, D. I. (2003) Uniqueness of *ab initio* shape determination in small-angle scattering. *J. Appl. Crystallogr.* **36**, 860–864
70. Norris, M., Fetler, B., Marchant, J., and Johnson, B. A. (2016) NMRfX processor: A cross-platform NMR data processing program. *J. Biomol. NMR* **65**, 205–216
71. Lanzetta, P. A., Alvarez, L. J., Reinach, P. S., and Candia, O. A. (1979) An improved assay for nanomole amounts of inorganic phosphate. *Anal. Biochem.* **100**, 95–97
72. Hung, K. W., Chang, Y. W., Eng, E. T., Chen, J. H., Chen, Y. C., Sun, Y. J., Hsiao, C. D., Dong, G., Spasov, K. A., Unger, V. M., and Huang, T. H. (2010) Structural fold, conservation and Fe(II) binding of the intracellular domain of prokaryote FeoB. *J. Struct. Biol.* **170**, 501–512
73. Veloria, J., Shin, M., Devkota, A. K., Payne, S. M., Cho, E. J., and Dalby, K. N. (2019) Developing colorimetric and luminescence-based high-throughput screening platforms for monitoring the GTPase activity of ferrous iron transport protein B (FeoB). *SLAS Discov.* **24**, 597–605